18th AIAA/CEAS Aeroacoustics Conference (33rd AIAA Aeroacoustics Conference)
04 - 06 June 2012, Colorado Springs, CO

AIAA 2012-2066

Development of semi-implicit Runge-Kutta schemes and application to a turbulent channel flow

Francois Kremer*, Christophe Bogey† and Christophe Bailly‡
Laboratoire de Mécanique des Fluides et d'Acoustique
UMR CNRS 5509, Ecole Centrale de Lyon
69134 Ecully Cedex, France

In this paper, two semi-implicit Runge-Kutta algorithms are developed for the simulation of wall-bounded flows. Using these schemes, the time integration is performed in an implicit way in the wall-normal direction, and in an explicit way in the other directions, in order to relax the time step constraint due to the fine mesh size at the wall. Based on analysis in the Fourier space and on results obtained for acoustic test cases, the semi-implicit schemes are shown to be of order 3 and to provide low dissipation and low dispersion. The accuracy of the schemes is compared with that of other schemes of the litterature. They are found to be at least as accurate as the standard Runge-Kutta algorithm of order 4. An LES of a turbulent channel flow at a friction Reynolds number of 360 and a Mach number of 0.1 is also carried out with one of the semi-implicit algorithms. In this case, a reduction of the computational time by a factor 1.33 with respect to an explicit scheme is obtained. Wall pressure and velocity spectra from the LES are presented to give insights into the turbulent structures developing in the flow. In particular, acoustic components are identified in the wavenumber-frequency spectra of wall pressure fluctuations.

I. Introduction

In the field of computational aeroacoustics (CAA), the development of direct noise computation (DNC) has drawn attention to the need of highly accurate numerical schemes for spatial and temporal discretisation. Indeed, the DNC approach relies on the computation of both the aerodynamic and acoustic fields, by solving the compressible Euler or Navier-Stokes equations. Since the acoustic fluctuations are by several orders of magnitude lower than the mean flow, and since these fluctuations are propagated over long distances, the numerical methods must ensure a good accuracy, and must generate low dissipation and low dispersion errors, in order to avoid the corruption of the acoustic field. These constaints become more stringent in the presence of solid boundaries in the case of wall-bounded flows. These flows are of significant interest in CAA. In particular, the attention has been drawn to wall-pressure fluctuations, because they are responsible for the noise radiated indirectly inside the cabin of vehicules such as cars or aircraft, as well as the noise emitted directly in the flow over a solid boundary.[1]

In the development of numerical methods for CAA problems, the usual approach is to consider the spatial and time discretization separately. Spatial discretization methods for aeroacoustics have been proposed for instance by Tam & Webb,[2] Lele[3] and Bogey *et al.*[4] When a discretization scheme is applied to the spatial derivatives of the Euler or Navier-Stokes equations, they reduce to the so-called semi-discretized form, which corresponds to an ordinary differential equation (ODE) $du/dt = F(u)$, with u the flow variable vector. Since the early papers of Runge[5] and Bashforth & Adams[6] published in the 19th century, two main families of methods have emerged to solve ODEs : the linear multistep methods and the Runge-Kutta (RK) methods, respectively. Both are used in CAA, but it can be noted that several explicit RK methods have been developed, for instance by Bogey *et al.*,[4] Hu *et al.*,[7] Stanescu & Habashi[8] and Berland *et al.*[9] These high-order methods have been optimized in the Fourier space, in order to minimize dissipation and dispersion

*PhD student, Email: francois.kremer@ec-lyon.fr
†CNRS Research Scientist
‡Professor at Ecole Centrale de Lyon & at Institut Universitaire de France

errors up to frequencies close to the cut-off frequency imposed by the time step. In wall-bounded simulations in particular, the mesh is usually strongly refined close to the wall, which might lead to a severe reduction of the time step to avoid stability problems. The use of an implicit scheme, which is stable for much larger time steps, is a possibility. However, it implies the inversion of massive linear systems, hence a high computational cost.

An alternative is to combine an implicit scheme with an explicit scheme. The time integration of terms involving derivatives in the wall-normal direction, where a fine mesh is implemented, is treated implicitly, while the time integration of the other terms is treated explicitly. Thus, the constraint on the time step is relaxed, and the computational cost due to the linear system inversion remains acceptable. This strategy has already been used by several authors in direct numerical simulation (DNS) of wall-bounded incompressible flows.[10,11] For example, in the DNS of a turbulent boundary layer, Wu & Moin[10] used a second-order Crank-Nicholson scheme to compute convection and diffusion terms involving derivatives in the wall-normal direction, while the other terms were treated with a third-order explicit Runge-Kutta scheme. These simulations aim to compute the aerodynamic field by solving the incompressible Navier-Stokes with methods, such as the fractional step method, in which a time accuracy of order 2 may be sufficient. The arbitrary combination of different time integration schemes might in addition lead to significant coupling errors. Therefore, approaches such as that of Wu & Moin may not be suited to DNC, and semi-implicit schemes must be developed specifically for that. A large number of papers can be found on so-called partitioned methods,[12–15] which propose combination of Runge-Kutta schemes appropriate for the integration of Convection-Diffusion-Reaction (CDR) equations. One of these methods, developed by Zhong,[14] has been for example used by Suh *et al.*[16] to perform compressible LES of wall-bounded flows. These methods are designed for the implicit time integration of diffusion or reaction terms, but not for the implicit integration of convection terms involving one selected direction. Nevertheless, they provide an interesting theoretical background for development of partitioned methods for aeroacoustic problems. Note that Kennedy & Carpenter[15] provided an extensive review of the requirements and methodologies for the development of semi-implicit Runge-Kutta schemes up to order 5.

In the present paper, the strategy used by the authors mentioned above is applied to the constraints of DNC, allowing to develop semi-implicit Runge-Kutta methods adapted to simulation of wall-bounded flows. These methods perform the time integration of terms involving wall-normal derivatives in an implicit way, while the other terms are integrated in an explicit way. The designed algorithms combine the explicit six-stage fourth-order RK scheme of Berland *et al.*[9] with original implicit RK schemes. The resulting methods are six-stage third-order semi-implicit Runge-Kutta schemes, referred to as SIRK63 in what follows. The dispersion and dissipation properties of the schemes are studied in the Fourier space, and comparison is made with the properties of the semi-implicit scheme of Zhong and the standard explicit RK scheme of order 4. The case of an acoustic pulse propagating in a 2-D domain is then considered in order to evaluate the accuracy of these schemes. Finally, one of the SIRK63 schemes is used in the large-eddy simulation (LES) of a turbulent channel flow at a Mach number $M = 0.1$ and a friction Reynods number $Re_\tau = 360$, based on the half-width of the channel and the friction velocity. To illustrate the quality of LES performed with the proposed SIRK63 algorithm on this canonical case of wall-bounded flows, two important topics of wall turbulence are addressed. The first one is the scaling of near-wall turbulent structures, which have been studied by many authors, as for instance Tomkins & Adrian[17] for boundary layers, and Jiménez *et al.*[18] for channel flows. The second one is closer to CAA applications, because it deals with the noise radiated directly by the wall pressure fluctuations. This problem has extensively been explored through theoretical studies using acoustic analogy,[19–21] and incompressible direct numerical simulations,[22,23] but only a few studies based on DNC can be found.[16,24]

The paper is organized as follows. First, the developement of the semi-implicit schemes is presented in section II, along with 2-D test cases to compare their accuracy with that of existing schemes. Then a 3-D turbulent channel flow simulated with one proposed semi-implicit scheme is described and turbulent structures and wall pressure fluctuations are analysed in section III. Concluding remarks are finally given in section IV.

II. Development of semi-implicit schemes

II.A. Formulation

The 2-D Euler equations are considered in the present study.

$$\frac{\partial u}{\partial t} = -\frac{\partial E_x}{\partial x} - \frac{\partial E_y}{\partial y} \tag{1}$$

where u is the vector containing the flow variables, and E_x and E_y are the Eulerian fluxes in the x et y directions, respectively. The equation is discretized in space, and the spatial derivatives are approximated by finite differences, yielding the following semi-discretized equations

$$\frac{\partial u}{\partial t} = f(u) + g(u) \tag{2}$$

with

$$[f(u)]_{i,j} = -\frac{1}{\Delta x} \sum_{l=-N}^{M} \alpha_l \, [E_x]_{i+l,j}$$

$$[g(u)]_{i,j} = -\frac{1}{\Delta y} \sum_{l=-N}^{M} \alpha_l \, [E_y]_{i,j+l}$$

where (i, j) are the indices of the mesh, $(\alpha_l)_{l=-N,M}$ are the coefficients of the finite-difference scheme, and Δx and Δy are the mesh spacings in the x- and y-direction, respectively. The case of a mesh strongly refined in one direction, as usually encountered in wall-bounded flows, is considered by assuming that $\Delta y \ll \Delta x$, so that the time integration of the term $g(u)$ raises stability concerns.

Following the strategy of Kennedy & Carpenter,[15] the time integration of the equation (2) is carried out with a s-stage semi-implicit RK scheme, which is expressed as

$$\begin{aligned} u_i &= u_n + \Delta t \textstyle\sum_{j=1}^{i-1} a_{ij}^{[E]} f(u_j) + \Delta t \sum_{j=1}^{i} a_{ij}^{[I]} g(u_j) \quad \text{for } 1 \le i \le s \\ u_{n+1} &= u_n + \Delta t \textstyle\sum_{i=1}^{s} b_i^{[E]} f(u_i) + \Delta t \sum_{i=1}^{s} b_i^{[I]} g(u_i) \end{aligned} \tag{3}$$

where $u_n = u(t)$, $u_{n+1} = u(t + \Delta t)$, Δt is the time step, u_i represents the flow variable vector at the stage i, $(a_{ij}^{[I]}, b_i^{[I]})$ are the coefficients of the implicit part of the scheme, performing the time integration of $g(u)$, and $(a_{ij}^{[E]}, b_i^{[E]})$ are the coefficients of the explicit part, for the time integration of $f(u)$. The design of a s-stage SIRK method consists of the choice of all these $s(s + 3)$ coefficients.

II.B. Development of the scheme

In the present study, the coefficients of the explicit part of the algorithm $(a_{ij}^{[E]}, b_i^{[E]})$ are chosen to be equal to those of the explicit fourth-order six-stage Runge-Kutta scheme of Berland *et al.*,[9] in order to take advantage of its good stability and accuracy properties. The number of stages of the semi-implicit method is thus fixed to $s = 6$. The aim of the following work is to determine the set of $s(s + 3)/2 = 27$ coefficients of the implicit part $(a_{ij}^{[I]}, b_i^{[I]})$. Stability and accuracy constraints will be defined first. Then the determination of the coefficients will be described.

II.B.1. Order of the implicit part

A fourth-order accuracy is imposed to the implicit part of the scheme by applying to the coefficients $(a_{ij}^{[I]}, b_i^{[I]})$ the classical order conditions (for the sake of clarity, the coefficients are given without the superscript [I])

$$\begin{array}{llll} (O1) & \sum_{i=1}^{s} b_i = 1 & (O2) & \sum_{i=1}^{s} b_i c_i = \frac{1}{2} \\ (O3)a & \frac{1}{2} \sum_{i=1}^{s} b_i c_i^2 = \frac{1}{3!} & (O3)b & \sum_{i,j=1}^{s} b_i a_{ij} c_j = \frac{1}{3!} \\ (O4)a & \frac{1}{6} \sum_{i=1}^{s} b_i c_i^3 = \frac{1}{4!} & (O4)b & \sum_{i,j=1}^{s} b_i c_i a_{ij} c_j = \frac{3}{4!} \\ (O4)c & \frac{1}{2} \sum_{i,j=1}^{s} b_i a_{ij} c_j^2 = \frac{1}{4!} & (O4)d & \sum_{i,j,k=1}^{s} b_i a_{ij} a_{jk} c_k = \frac{1}{4!} \end{array} \tag{4}$$

with $c_i^{[I]} = \sum_{j=1}^{i} a_{ij}^{[I]}$.

II.B.2. Coupling conditions for order 3

Assuming that the conditions (4) are satisfied, the order of the whole semi-implicit scheme is now considered. It must be noted that the fourth order of both implicit part and explicit part is not sufficient to obtain the fourth order of the entire SIRK scheme. Indeed, the time discretization error exhibits coupling terms of lower order. These terms are exactly the sums appearing in the order conditions (4), but with the coefficients of both the explicit and implicit parts. For example, to obtain a semi-implicit scheme of order 2, coupling terms of order 1 must be cancelled by imposing the following coupling conditions :

$$\begin{array}{ll} (C2)a & \sum_{i=1}^{s} b_i^{[E]} c_i^{[I]} = \frac{1}{2} \\ (C2)b & \sum_{i=1}^{s} b_i^{[I]} c_i^{[E]} = \frac{1}{2} \end{array} \tag{5}$$

The cancellation of all coupling terms is tricky since their number grows rapidly with the desired order.[15] There are 2 terms associated with order 2, 10 terms with order 3, and 44 terms with order 4. Developing a semi-implicit scheme of order 4 implies to impose 56 coupling conditions, which is here impossible with the set of 27 coefficients. If the simplifying assumption

$$b_i^{[I]} = b_i^{[E]} = b_i \quad \text{for } 1 \leq i \leq s \tag{6}$$

is imposed, a large number of coupling conditions vanish, in the sense that they become equivalent to other conditions which are already satisfied. For instance, condition (C2)a in (5) becomes equivalent to the order condition (O2) in (4), and condition (C2)b becomes equivalent to an order condition verified by the explicit part of the scheme. Some of the third order coupling conditions also vanish, and only three of them remain :

$$\begin{array}{ll} (C3)a & \frac{1}{2}\sum_{i=1}^{s} b_i c_i^{[E]} c_i^{[I]} = \frac{1}{3!} \\ (C3)b & \sum_{i,j=1}^{s} b_i a_{ij}^{[E]} c_j^{[I]} = \frac{1}{3!} \\ (C3)c & \sum_{i,j=1}^{s} b_i a_{ij}^{[I]} c_j^{[E]} = \frac{1}{3!} \end{array} \tag{7}$$

with $c_i^{[E]} = \sum_{j=1}^{i-1} a_{ij}^{[E]}$. It can be noted that the order condition of the implicit part (O1) in (4) also vanishes, because it becomes equivalent to an order condition of the explicit part.

Thus, imposing the conditions (4), (6) and (7) allows to design a semi-implicit scheme of order 3.

II.B.3. Coupling conditions for order 4

It is assumed that the conditions (4), (6) and (7) are respected. The simplifying assumption (6) also reduces the number of fourth order coupling conditions, but there still remains a number of eighteen. Another assumption can reduce their number again. Indeed, by imposing

$$c_i^{[I]} = c_i^{[E]} = c_i \quad \text{for } 1 \leq i \leq s \tag{8}$$

all conditions (C3) in (7) vanish, and only two fourth order coupling conditions remain :

$$\begin{array}{ll} (C4)a & \sum_{i,j,k=1}^{s} b_i a_{ij}^{[I]} a_{jk}^{[E]} c_k = \frac{1}{4!} \\ (C4)b & \sum_{i,j,k=1}^{s} b_i a_{ij}^{[E]} a_{jk}^{[I]} c_k = \frac{1}{4!} \end{array} \tag{9}$$

It must be noted that due to (8), the first stage of the implicit part is explicit. Indeed, for $i = 1$, the simplifying assumption yields $a_{11}^{[I]} = c_1^{[I]} = c_1^{[E]} = a_{11}^{[E]} = 0$.

II.B.4. Stability

In the present study, the stability is studied with the same approach as Hu *et al.*[7] The 2-D wave equation,

$$\frac{\partial u}{\partial t} = c\left(\frac{\partial u}{\partial x} + \frac{\partial u}{\partial y}\right) \tag{10}$$

with c the speed of sound, is considered. The spatial derivatives are discretized with a central finite difference scheme and a 2-D Fourier transform is applied to (10). Defining the effective wavenumbers k_x^* and k_y^* by

$$k_\xi^* \Delta\xi = 2\sum_{l=1}^{N} \alpha_l \sin(l k_\xi \Delta\xi) \quad \xi = x, y \tag{11}$$

with $(\alpha_l)_{l=1,N}$ the coefficients of the finite-difference scheme, Δx and Δy the mesh spaces, and k_x and k_y the exact wavenumbers in the x- and y-direction, the following equation is obtained :

$$\frac{\partial \tilde{u}}{\partial t} = (\mathrm{i}ck_x^* + \mathrm{i}ck_y^*)\tilde{u} \tag{12}$$

with $\tilde{u}$ the spatial Fourier transform of u and $\mathrm{i} = \sqrt{-1}$. Considering that a SIRK scheme is used to integrate this equation, with the term $\mathrm{i}ck_x^*\tilde{u}$ treated by the explicit part of the scheme, and $\mathrm{i}ck_y^*\tilde{u}$ treated by the implicit part, it can be shown that the amplification factor at each time step is given by the linear stability function[13]

$$R(z_x, z_y) = \frac{\tilde{u}_{n+1}}{\tilde{u}_n} = \frac{Det[\mathbf{I} - z_x\mathbf{A}^{[E]} - z_y\mathbf{A}^{[I]} + (z_x + z_y)\mathbf{1} \otimes \mathbf{b}^T]}{Det[\mathbf{I} - z_y\mathbf{A}^{[I]}]} \tag{13}$$

where $\tilde{u}_n = \tilde{u}(t)$, $\tilde{u}_{n+1} = \tilde{u}(t + \Delta t)$, $z_x = \mathrm{i}ck_x\Delta t$, $z_y = \mathrm{i}ck_y\Delta t$, $\mathbf{A}^{[E]} = a_{ij}^{[E]}$, $\mathbf{A}^{[I]} = a_{ij}^{[I]}$, $\mathbf{b} = b_i$, $\mathbf{1} = \{1, 1, ..., 1\}$, and $\mathbf{I}$ is the identity matrix. It is assumed in this formula that the assumption (6) is respected. The semi-implicit algorithm is stable for all couples of (z_x, z_y) yielding $|R| \leq 1$. Note that the amplification factor of the explicit part and of the implicit part of the algorithm are given by $R(z_x, 0)$ and $R(0, z_y)$, respectively. One important requirement is to ensure that the implicit part is unconditionally stable, hence

$$|R(0, z_y)| \leq 1 \qquad \text{for } z_y \in \mathrm{i}\mathbb{R} \tag{14}$$

The unconditional stability is quite difficult to obtain with an arbitrary set of the coefficients $(a_{ij}^{[I]}, b_i^{[I]})$. To deal with this problem, a singly-diagonally structure is imposed to the coefficients :

$$a_{ii}^{[I]} = \gamma \qquad \text{for } 1 \leq i \leq s \tag{15}$$

with γ a free parameter. Singly-diagonally implicit RK methods[25] (SDIRK) show interesting results for stability. For example, Kennedy & Carpenter[15] gave an interval of γ for the development of a 6-stage semi-implicite RK scheme ensuring (14). It must be noted that, in the present study, the assumption (8) implies $a_{11}^{[I]} = 0$. In this case, the condition (15) is limited to $2 \leq i \leq s$.

II.B.5. Determination of the coefficients $(a_{ij}^{[I]}, b_i^{[I]})$

Now that the constraints ensuring accuracy and stability are defined, the $s(s+3)/2 = 27$ coefficients of the implicit part are computed. The following approach is used. First, a value of γ ensuring condition (14) is chosen. Second, some of the accuracy conditions (order, simplifying assumptions) are chosen, and a set of coefficients respecting these conditions is computed. Finally, the linear stability function (13) is evaluated so that the constructed SIRK scheme is stable for a range of (z_x, z_y) as wide as possible.

It appears that obtaining a semi-implicit scheme which exhibits both high accuracy and high stability is difficult. Therefore, it has been chosen to compute two different sets of the coefficients $(a_{ij}^{[I]}, b_i^{[I]})$, focusing on either the stability or the accuracy. Hence, two semi-implicit Runge-Kutta algorithm are proposed. The one with enforced stability is referred to as SIRK63-S, and the one with enforced accuracy is referred to as SIRK63-A. The constraints used in the computation of the coefficients $(a_{ij}^{[I]}, b_i^{[I]})$ are given in the table 1 for the two proposed schemes.

Table 1. Constraints imposed to the coefficients of the implicit part of the SIRK63 schemes

	SIRK63-S	SIRK63-A
SDIRK structure	$a_{ii}^{[I]} = \gamma = 0.41$	$a_{ii}^{[I]} = \gamma = 0.245$
simplifying assumptions	$b_i^{[I]} = b_i^{[E]}$	$b_i^{[I]} = b_i^{[E]}$ and $c_i^{[I]} = c_i^{[E]}$
order of the implicit part	(O2), (O3)a-b, (O4)a-d	(O2), (O3)a-b, (O4)a-d
coupling conditions	(C3)a-c	(C4)a

It can be seen that the order of SIRK63-S is limited to 3. The algorithm exhibits a high stability, as it will be seen later from the results of test cases. For the SIRK63-A scheme, the simplifying assumptions (6) and (8) are sufficient to obtain the order 3 without the (C3) conditions, as expected. It has been attempted to reach the order 4, but no set of coefficients respecting (C4)a and (C4)b has been found. Condition (C4)a only has been imposed, so the time accuracy remains of order 3. However, the condition (C4)a leads to the cancellation of some terms of order 3 in the time discretization error, so that its magnitude is reduced, which will be shown in the next section.

II.C. Dissipation and dispersion properties of the schemes

The dissipation and dispersion properties of the implicit part and explicit part of the SIRK63 algorithms are evaluated in the present section. It has been seen above that the amplification factor of the implicit part of a SIRK algorithm is given by $R(0, \mathrm{i}ck_y^*\Delta t)$. Thus, by defining $\omega = ck_y^*$ and $G(\omega\Delta t) = |G|e^{\mathrm{i}\omega^*\Delta t} = R(0, \mathrm{i}\omega\Delta t)$, the damping factor of the implicit part is given by $1 - |G|$ and its dispersion error by $|\omega^*\Delta t - \omega\Delta t|/\pi$. The damping factor and the dispersion error of the explicit part are obtained in the same manner with $R(\mathrm{i}ck_x^*\Delta t, 0)$.

Figure 1(a) shows the damping factor, as a function of nondimensional angular frequency $\omega\Delta t$, of the implicit part of the proposed SIRK63-A and SIRK63-S methods, as well as that of the implicit part of the ASIRK-3C scheme of Zhong.[14] The damping factor of the standard explicit fourth-order Runge-Kutta scheme (RK4) is also given as a reference. The scheme of Zhong appears more dissipative than the proposed schemes. Its damping factor is by one order of magnitude higher than that of RK4 for $\omega\Delta t < \pi/4$. In the same range of frequencies, the proposed SIRK63-S has a dissipation close to that of RK4. It is even slightly more accurate for $\omega\Delta t > \pi/4$. The other scheme, SIRK63-A, specifically developed for accuracy, shows a damping factor by two orders of magnitude lower than that of SIRK63-S for the whole range of frequencies.

The dispersion error $|\omega^*\Delta t - \omega\Delta t|/\pi$ given in figure 1(b) shows a behavior similar to that observed on the damping factor. The implicit part of the scheme of Zhong is more dispersive than the proposed ones. Again, the implicit part of SIRK63-A is more accurate than that of SIRK63-S for $\omega\Delta t < \pi/4$. For higher frequencies, the dispersion of the two schemes are close.

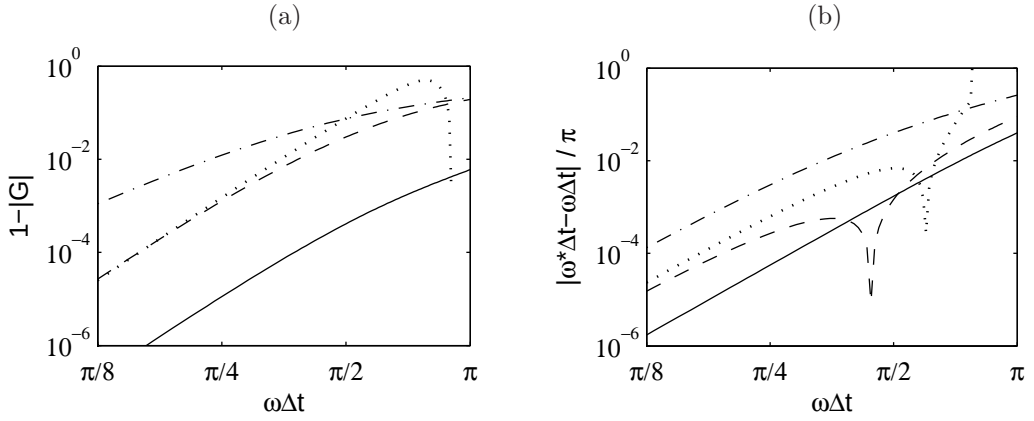

Figure 1. (a) Damping factor, and (b) dispersion error per time step of the implicit part of the schemes, as a function of nondimensional frequency. — · — · ASIRK-3C of Zhong, ····· standard RK4, proposed schemes: ——— SIRK63-A, — — — SIRK63-S.

The damping factor is plotted as a function of the nondimensional angular frequency $\omega\Delta t$ in figure 2(a) for the explicit part of the different schemes. The scheme of Zhong presents the higher error again. The two proposed SIRK63 schemes have the same explicit part : the scheme RK46-Ber of Berland *et al.*[9] It has a damping factor by two orders of magnitude lower than that of RK4 for the whole range of frequencies. The dispersion error, given in figure 2(b), exhibits roughly the same tendencies. Finally, the present study shows that the accuracy of the semi-implicit schemes proposed in this paper is higher than that of the semi-implicit scheme of Zhong, and at least as good as that of the standard RK4 scheme.

II.D. Test cases

II.D.1. Definition

The properties of the semi-implicit schemes are studied for the propagation of an acoustic pulse without mean flow. The 2-D Euler equations are solved on an anistropic cartesian mesh. The aspect ratio is defined as $\mathrm{AR} = \Delta x/\Delta y$ where Δx and Δy are the mesh spacings in the x and y directions, respectively. When Δx is fixed, the higher the value of AR is, the finer the mesh in the y direction. The mesh thus contains $140 \times \mathrm{AR}.140$ points. The initial conditions are defined as :

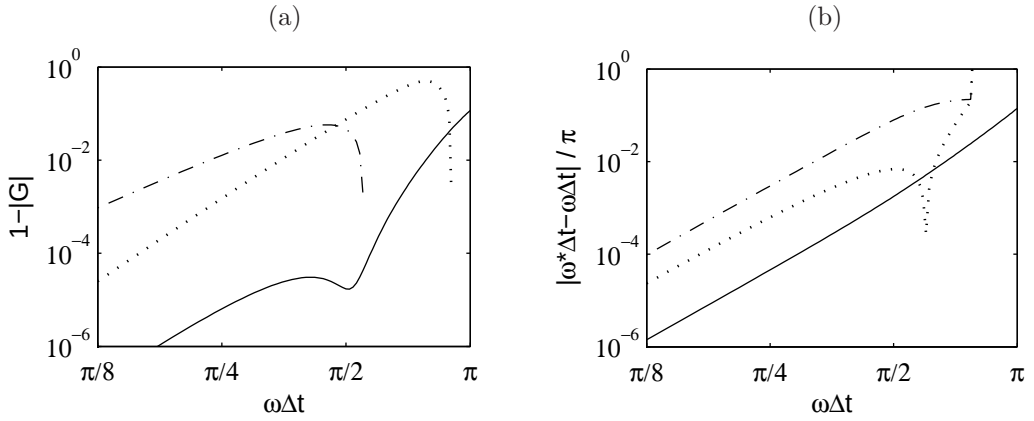

Figure 2. (a) Damping factor, and (b) dispersion error per time step of the explicit part of the schemes, as a function of nondimensional frequency. – · – · – ASIRK-3C of Zhong, ····· standard RK4, ——— proposed SIRK63-A and SIRK63-S : RK46-Ber of Berland *et al.*

$$\begin{aligned} p &= p_0 + \Delta p.exp[-ln2(x^2+y^2)/b^2] \\ \rho &= \rho_0 + (p-p_0)/c^2 \\ u_x &= u_y = 0 \end{aligned} \tag{16}$$

where $b = 3\Delta x$, $p_0 = 10^5\ Pa$, $\Delta p = 10\ Pa$, $c = \sqrt{\gamma p_0/\rho_0}$, $\rho_0 = p_0/(T_0(\gamma-1)C_v)$, $T_0 = 293\ K$ and $C_v = 717.5\ J.K^{-1}$. In order to compare the accuracy of the different time integration schemes properly, the spatial discretisation error must be negligible with respect to the time integration error. Therefore, a 21-point centered finite-difference scheme of order 20 is used. For the stability test cases shown in the next section, periodic conditions are applied to the boundaries of the domain, such that the centered finite-difference scheme can be used in the entire mesh.

Simulations are carried out with the following time integration schemes: SIRK63-S, SIRK63-A, ASIRK-3C and RK4. They are tested for aspect ratios of 2, 4, 8, 16 and 32, with Δx being fixed and Δy varying. The semi-implicit schemes are implemented in such a way that the terms containing y-derivatives in the Euler equations are integrated by the implicit part of the SIRK algorithm, while the other terms are integrated with the explicit part. The CFL number is defined as $\text{CFL} = c\Delta t/\Delta x$.

II.D.2. Stability

The aim of the stability test is to find the maximum CFL number, CFL_{max}, ensuring stability. The values of CFL_{max} are plotted in figure 3 as a function of AR, for the different schemes. The axes are in logarithmic scale. Using the explicit RK4 scheme, the maximum CFL number decreases, as expected, as the aspect ratio increases, that is as Δy decreases. The scheme of Zhong exhibits a constant value of CFL_{max}, equal to 0.2. The maximum CFL number of the proposed SIRK63-A decreases as AR increases, then it stabilizes at $\text{CFL}_{max} = 0.25$ for $AR \geq 16$. Finally, SIRK63-S appears to be the most stable scheme, with $\text{CFL}_{max} = 1.2$ for all aspect ratios.

II.D.3. Accuracy

To evaluate the accuracy, simulations are carried out up to $t = 32\Delta x/c$, with c the speed of sound, for CFL numbers varying from 0.1 to 1. The results are compared with reference simulations. Since the grids are not identical for the different aspect ratios, one reference simulation is run for each grid with a very small CFL number. For instance, the CFL number is equal to 10^{-1} for AR = 1 and to 10^{-4} for AR = 32. The reference solution computed on the grid with AR = 1 is given in figure 4.

The accuracy of the schemes is estimated by the global error, defined as follows :

$$E_{glob} = \frac{\sqrt{\iint_S (p-p_{ref})^2\ ds}}{\sqrt{\iint_S (p_{ref}-p_0)^2\ ds}} \tag{17}$$

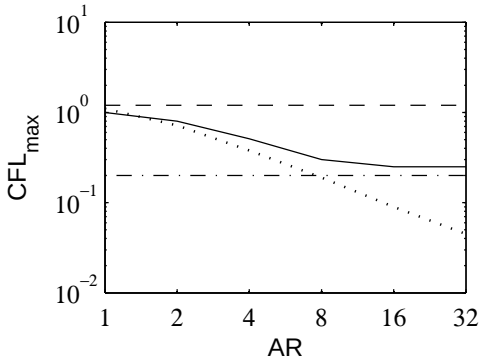

Figure 3. Maximum CFL number of the time integration schemes, as a fonction of aspect ratio AR $= \Delta x/\Delta y$. ASIRK-3C of Zhong, standard RK4, proposed schemes: SIRK63-A, SIRK63-S.

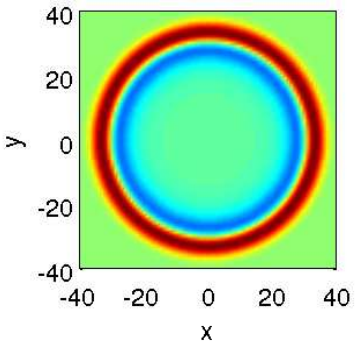

Figure 4. Fluctuating pressure field, at $t = 32\Delta x/c$, of the reference simulation for the acoustic pulse case, run with the RK4 time integration scheme, for AR $= 1$ and CFL $= 0.01$. The color scale ranges between ± 1 Pa.

where p_{ref} is derived from the reference solution. Figures 5(a) and (b) show the global error obtained for different schemes in the simulations with values of AR equal to 1 and 32, respectively. The axes are in logarithmic scales. The respective magnitudes of the global error obtained for the four schemes do not depend appreciably on the aspect ratio. The only difference is observed on the maximum CFL number of SIRK63-A and RK4. Therefore, the analysis of accuracy can be limited to the case AR = 1, given in figure 5(a). All the semi-implicit algorithms show a slope of order 3. The scheme of Zhong exhibits a weak accuracy, his error being by more than one order of magnitude higher than that of RK4. On the contrary, the proposed schemes have a good accuracy : that developed for stability, SIRK63-S, shows an error similar to that of RK4, and the error of that developed for accuracy, SIRK63-A, is by one order of magnitude lower.

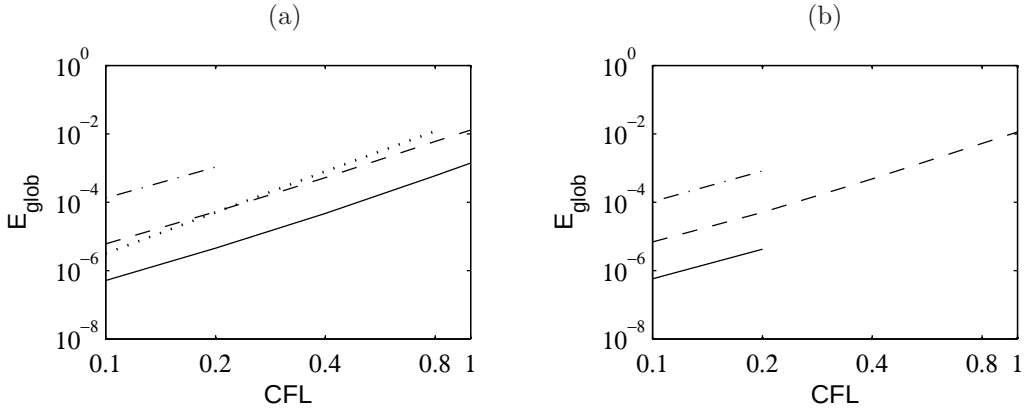

Figure 5. Global error E_{glob} of the time integration schemes, at $t = 32\Delta x/c$, for the acoustic pulse case: (a) AR=1, (b) AR=32. ASIRK-3C of Zhong, standard RK4, proposed schemes: SIRK63-A, SIRK63-S.

In order to highlight the coupling effect between the explicit and implicit parts of the SIRK algorithms, snapshots of the local error scaled by the global error, defined as $(p - p_{ref})/E_{glob}$, are shown in figure 6, for simulations performed with CFL = 0.1 and AR = 1. As expected, the error of the RK4 scheme in figure 6(a) is isotropic because the same algorithm is used in the x and y directions. Inversely, the error of the semi-implicit schemes exhibits anisotropy. The error of the scheme of Zhong, plotted in figure 6(b), is dominant in the directions parallel to the axes of the mesh, whereas the proposed SIRK63-A in figure 6(c) and SIRK63-S in figure 6(d) schemes provide the largest errors in the diagonal directions.

It must be noted that these error patterns can be different at other values of the CFL number and of AR. For instance, figure 7(a) show the local error of the SIRK63-S scheme at the same aspect ratio as above, but for CFL = 1. Compared to the error at CFL = 0.1 in figure 6(c), the pattern clearly changes. Besides, the influence of the aspect ratio is highlighted by the comparison of the figures 7(a) and (b), corresponding to AR = 1 and 32, for the same CFL number. It can be seen that the aspect ratio has no effect on the anistropy of the local error.

II.E. Summary

The properties of the schemes studied in this paper are summarized in the table 2, which reports the maximum CFL number and the global error at CFL = 0.2, for aspect ratios of 1 and 32. The developed semi-implicit schemes show greater stability and accuracy properties than that of the ASIRK-3C scheme of Zhong. The proposed SIRK63-S algorithm appears to be the more stable, with a maximum CFL number of 1.2 independent of the aspect ratio. Its accuracy is close to that of the standard RK4 scheme. The SIRK63-A scheme exhibits a low numerical error compared to that of RK4. Its maximum CFL number, although decreasing slightly with the aspect ratio, remains higher than that of the scheme of Zhong.

III. Simulation of a plane channel flow

III.A. Parameters

A channel flow at friction Reynolds number $Re_\tau = hu_f/\nu = 360$ and centerline Mach number $M_c = U_c/c = 0.1$ is considered, where h is the half-width of the channel, $u_f = \sqrt{\tau_w/\rho}$ is the friction velocity, based on the

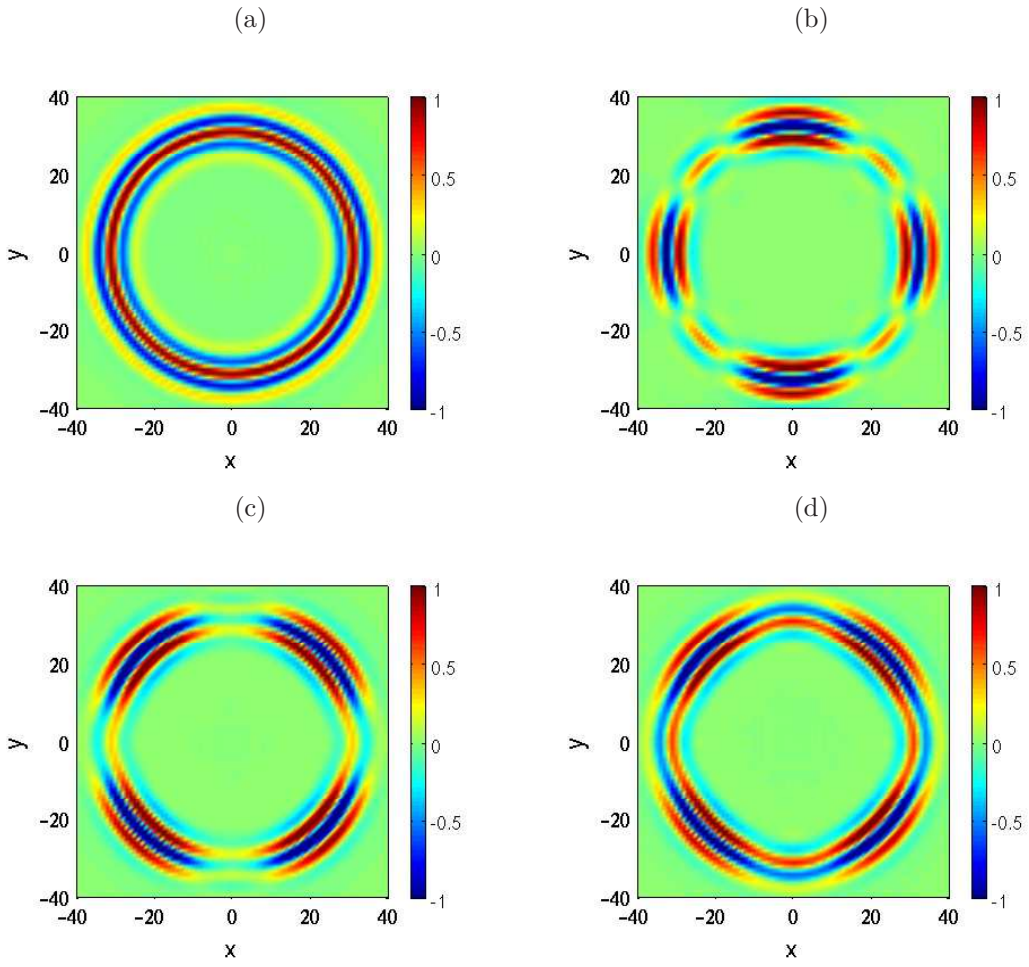

Figure 6. Local error $p - p_{ref}$ scaled by the global error E_{glob}, at $t = 32\Delta x/c$, of simulations CFL= 0.1 and AR= 1 : (a) standard RK4, (b) ASIRK-3C of Zhong, proposed schemes: (c) SIRK63-S, (d) SIRK63-A

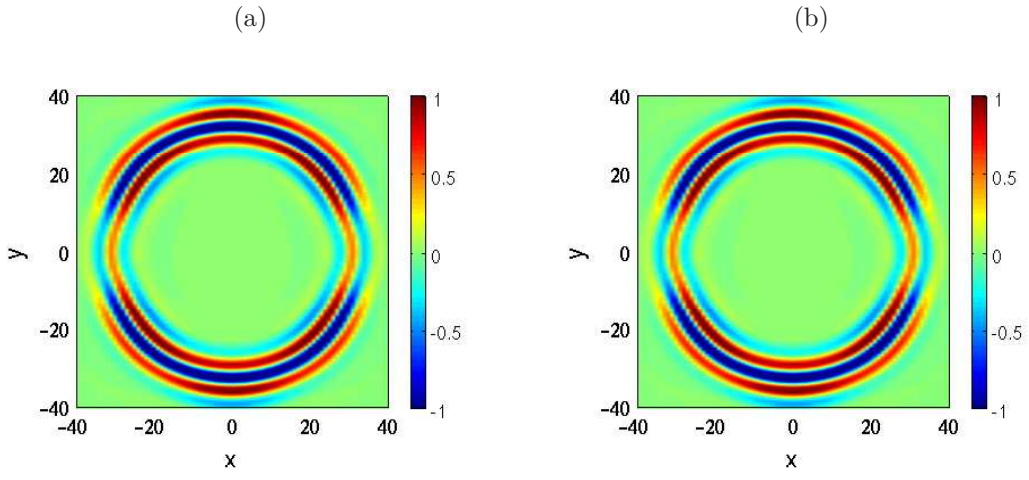

Figure 7. Local error $p - p_{ref}$ scaled by the global error E_{glob}, at $t = 32\Delta x/c$, of simulations run with the proposed SIRK63-S: (a) AR=1, (b) AR=32

Table 2. Comparison of the maximum CFL numbers, and of the global error of the schemes, as a function of the aspect ratio.

	CFL_{max}		E_{global} (CFL = 0.2)	
	AR = 1	AR = 32	AR = 1	AR = 32
SIRK63-S	**1.2**	**1.2**	4.9×10^{-5}	5.0×10^{-5}
SIRK63-A	1.0	0.25	$\mathbf{4.1 \times 10^{-6}}$	$\mathbf{4.2 \times 10^{-6}}$
ASIRK-3C	0.2	0.2	8.2×10^{-4}	8.2×10^{-4}
RK4	1.1	0.045	4.4×10^{-5}	–

wall shear stress τ_w and the density ρ, ν is the kinematic molecular viscosity, U_c is the centerline velocity and c is the speed of sound. The dimensions of the channel $L_x \times L_y \times L_z = 12h \times 2h \times 6h$ are imposed.

At time $t = 0$, laminar Blasius profiles with thickness $\delta_0 = 0.4h$ have been imposed for the streamwise velocity at each wall. Spanwise and wall-normal velocities are set to zero. Static pressure and temperature are uniform over the whole domain, with $p_0 = 10^5\ Pa$ and $T_0 = 293\ K$. The flow is driven by a mean pressure gradient, which is given by a body force in the streamwise direction ρf, with $f = \tau_w/(\rho h)$. The transition to turbulent flow is triggered by adding velocity fluctuations in the Blasius velocity profiles, following a method initially developed by Bogey *et al.* for pipe flows.[29]

III.B. Numerical methods

The LES is performed by solving the compressible Navier-Stokes equations, using low-dissipation and low-dispersion 11-points finite differences for spatial derivatives.[4] Periodic boundary conditions are implemented in the x (streamwise) and z (spanwise) directions. In the y (wall normal) direction, a no-slip boundary condition is imposed. The dissipative effects of the subgrid motions are taken into account by the use of an explicit filter of order 6, removing the smallest discretized scales, while leaving the well-resolved scales nearly unaffected.[30] The simulation is carried out on a Cartesian grid, with constant mesh spacings in the streamwise and spanwise directions, equal to $\Delta x^+ = 16.6$ and $\Delta z^+ = 8.3$ in wall units. In the wall normal direction, the mesh spacing is stretched with a constant expansion rate r = 1.0442, yielding values of Δy^+ from 0.95 at the walls to 15.8 at the center of the channel. The numbers of grid points in each direction is $n_x \times n_y \times n_z = 257 \times 133 \times 257 = 9.5$ million points.

The time integration is performed by the developed semi-implicit scheme SIRK63-S, which exhibits high stability properties. The implicit part is used to consider the convective terms involving y-derivatives, while the other terms are treated with the explicit part of the scheme. In order to distinguish the stability requirements in the different directions of the mesh, two CFL numbers are defined: $CFL_z = c\Delta t/\Delta z$, and $CFL_x = c\Delta t/\Delta x$. The time step is chosen such as $CFL_z = 1$ to ensure stability of the explicit part of the SIRK63-S algorithm, yielding a time step $\Delta t \approx 2.05 \times 10^{-7}$ s. Then, the maximum CFL number at which the implicit part of the scheme is used is reached at the walls, where $CFL_y = 8.7$. In order to reduce the CPU time, the semi-implicit scheme is applied to regions of the grid where $\Delta y < \Delta z$, corresponding to the regions close to the wall. Outside these regions, the value of CFL_y is smaller than 1, so that no implicit time integration is needed. Therefore, all the convective terms, including those containing y-derivatives, are integrated with the explicit RK46-Ber scheme.

The simulation is carried out on a shared-memory computer SGI ALTIX UV 1000. The CPU time of the algorithm has been compared with that of a fully-explicit simulation performed on the same case. For that simulation, the RK46-Ber scheme is used over the whole domain, with a CFL number $CFL_y = 1$ at the walls, yielding a time step $\Delta t \approx 2.37 \times 10^{-8}$ s. When the computation is run on a single core, the fully-explicit simulation is about 1.6 times faster than the semi-implicit one, which is severely penalized by the inversion of the linear systems. However, the semi-implicit algorithm becomes more efficient when the code is parallelized with the OpenMP library on several threads, since it exhibits a very good acceleration factor up to about 12 threads, as it can be seen on figure 8(a). Figure 8(b) shows the CPU time of the semi-implicit and fully-explicit algorithms, for a simulation over a physical time of 10^{-6} s. It can be seen that for a number of threads greater than 7, the semi-implicit algorithm becomes faster. With 12 threads, it exhibits a computational time about 1.33 times smaller than that of the fully-explicit algorithm. The LES has been finally performed with a code parallelized on 12 threads.

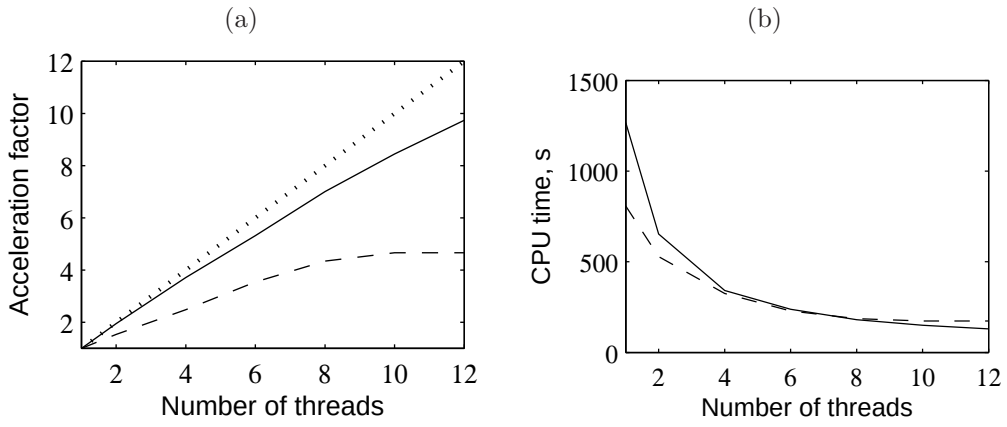

Figure 8. (a) Acceleration factor, and (b) CPU time for a simulation over a physical time of 10^{-6} s. — — — RK46-Ber ——— SIRK63-S

The good acceleration factor of the SIRK63-S scheme can be explained by a further analysis of how the semi-implicit algorithm works. At each stage l of the algorithm, the following system must be solved:

$$(\mathbf{I} - \gamma \Delta t \mathbf{J}_l)\mathbf{k} = \mathbf{X_l} \tag{18}$$

where $\mathbf{k}$ is the unknow vector, $\mathbf{X}_l$ is the vector containing the terms computed explicitly, $\mathbf{J}_l$ is the jacobian matrix of the terms computed implicitly, and $\mathbf{I}$ is the identity matrix. The dimension of this system is very large, since it is given by the number of degrees of freedom of the problem, equal to the number of grid points times the number of flow variables (5 for the compressible Navier-Stokes equations). However, since the terms integrated implicitly contain only the discretized $y-$ derivatives, they involve only one direction of the mesh. Then the global system (18) can be decomposed in several smaller systems:

$$(\mathbf{I} - \gamma \Delta t \mathbf{J}_l^{(i,k)})\mathbf{k}^{(i,k)} = \mathbf{X}_l^{(i,k)},\ \forall (i,k) \in [\![1, n_x]\!] \times [\![1, n_z]\!] \tag{19}$$

where (i,k) denotes the indices of the mesh in the x-, and z-direction. The dimension of these systems is reduced to $5 \times n_y$. The resolution of these $n_x \times n_z$ systems represents about 87% of the computationnal time when the code is executed sequentially. The important point is that each system is independent of each other, so that they can be solved simultaneously. Therefore, parallelization of the set of linear systems (19) yields no communication time. As the number of threads grows, the acceleration factor of the code remains very high, until the computational time due to the resolution of (19) becomes comparable to that of the other parts of the algorithm.

III.C. Flow field

Snapshots of the vorticity field in $x-y$ and $z-y$ planes are shown on figure 9(a) and (b), respectively. It can be seen that the turbulence is fully developed through the height of the channel. The near-wall regions exhibit structures of small size and intense vorticity, whereas the structures at the mid-heigh of the channel are less intense and greater in size.

Figures 10(a) and (b) present the mean streamwise velocity profile and streamwise fluctuation intensities, respectively, as functions of the distance to the wall. Wall scaling is used for the mean velocity $U^+ = U/u_\tau$, fluctuations intensities $u'^+ = \sqrt{\overline{u'u'}}/u_f$ and wall distance $y^+ = yu_f/\nu$. The wall distance is given in logarithmic scale. Data from the channel flow simulation at $Re_\tau = 395$ of Moser *et al.*[31] are also reported as a reference. A very good agreement is found for both mean and fluctuating velocities. The peak rms velocity is located at $y^+ = 13.2$.

III.D. Definition of spectra

For spectral analysis, data from the LES are stored over a time period of $T = 23h/U_c$. Including the time of the transition to a fully turbulent state, the total duration of the simulation is equal to $T_{total} = 70h/U_c$.

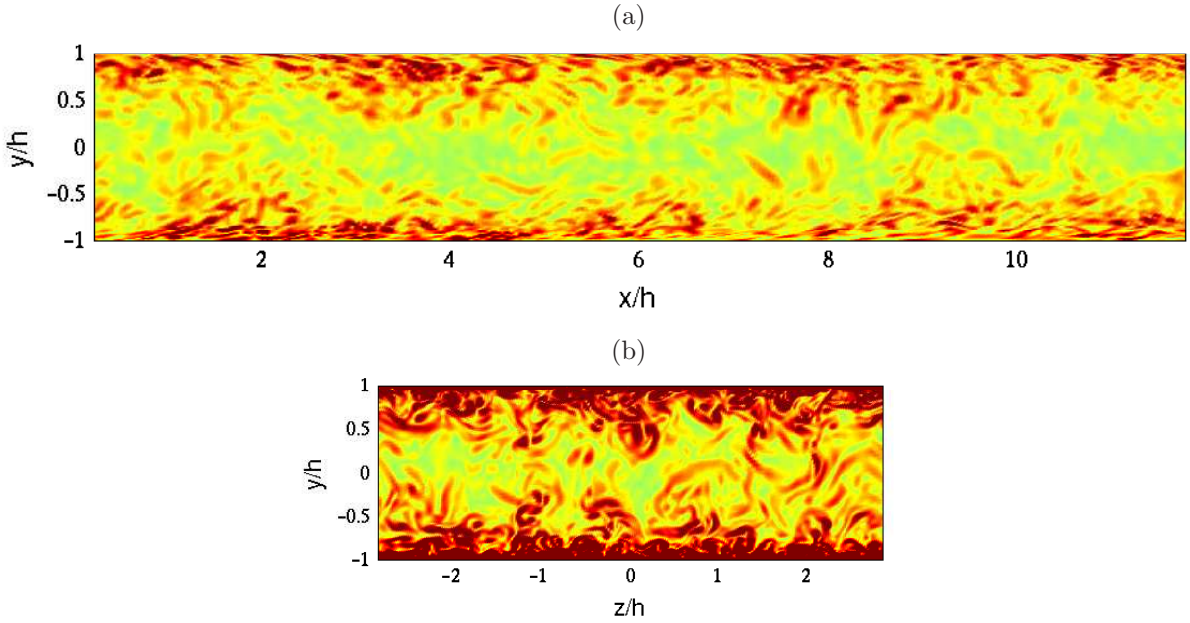

Figure 9. Snapshot of the vorticity norm. The color scale ranges up to $2 \times 10^4\ s^{-1}$. (a) $x-y$ plane, (a) $z-y$ plane.

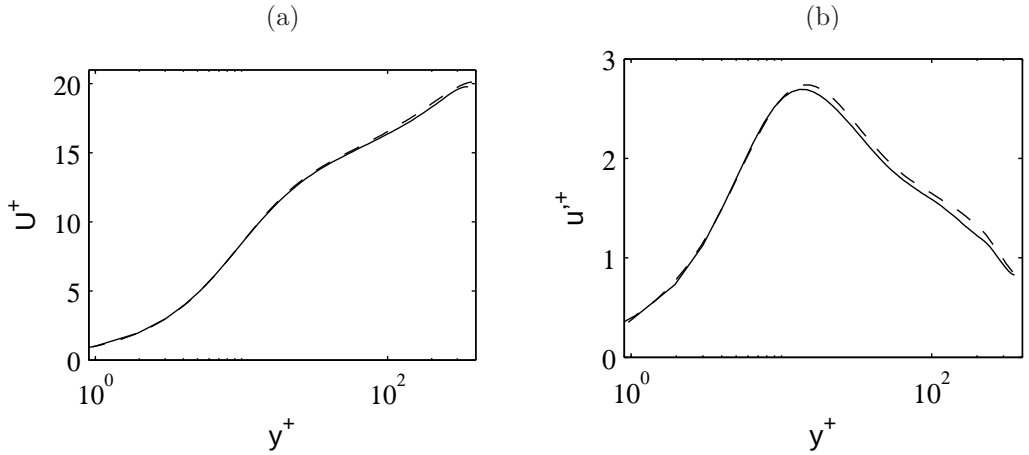

Figure 10. (a) Mean streamwise velocity $U^+ = U/u_\tau$, and (b) streamwise fluctuation intensities $u'^+ = \sqrt{\overline{u'u'}}/u_f$ as functions of the wall distance $y^+ = yu_f/\nu$. – – – DNS of Moser *et al.*[31] at $Re_\tau = 395$, ——— present LES.

Every 5^{th} time step, samples of pressure at the walls, and of velocity components in wall-parallel planes are collected. The location of these planes are $y^+ = 18$ and 105 in wall units, and $y/h = 0.05$ and 0.3 in outer units. The location of the first plane is close to that of the maximum rms velocity. Therefore, the database contains time-space samples, noted $q(x_i, z_j, t_n)$; $1 \leq i \leq n_x; 1 \leq j \leq n_z; 1 \leq n \leq N$, where $N = 2000$ is the number of time samples. The quantity q represents either the wall pressure, or a velocity component in one of the planes where data is collected. For each of these variables, a three-dimensional spectrum $\hat{q}(k_x, k_z, \omega)$ is obtained, as a function of streamwise and spanwise wavenumbers k_x and k_z, and angular frequency ω. Power spectral densities (PSD) are finally obtained as $\Phi_{qq} = \hat{q}\hat{q}^*/(L_x L_z T_S)$.

The frequency range is $0.014 \leq \omega^+ = \omega\nu/u_f^2 \leq 14.4$, and the wavenumber ranges are $0.0015 \leq k_x^+ = k_x\nu/u_f \leq 0.18$ and $0.0031 \leq k_z^+ = k_z\nu/u_f \leq 0.38$.

III.E. Turbulent structures

Figure 11(a) shows the power spectral densities of the three components of velocity in the plane located at $y^+ = 18$, as a function of the spanwise wavenumber, given in wall units $k_z^+ = k_z\nu/u_f$. The axes are in logarithmic scales. At low frequencies, the levels found in the spectrum for the wall-normal velocity are by two orders of magnitude lower than those for the spanwise velocity. The latter are by one order of magnitude lower than those for the streamwise velocity over the whole range of wavenumbers. These differences indicate the strong anisotropy of the velocity fluctuations in the near-wall region. The spectrum of the streamwise velocity spreads over a large range of wavenumbers, but the maximum is found at $k_z^+ \approx 0.02$. A peak is found also for the wall normal velocity component, around $k_z^+ = 0.05$. This spatial arrangement is a typical feature of the near-wall streaks, which consist in regions of high and low streamwise velocity elongated in the streamwise direction. These structures are arranged regularly in the spanwise direction, giving the observed peak in the spanwise spectrum. The streaks are accompanied by streamwise vortices, whose spanwise separation is twice smaller than that of the streaks. These vortices induce the peak visible in the spectrum of the wall normal velocity.

It can be noticed that the spanwise separation of the streaks is higher than the size of 100 wall units usually observed in the literature.[32] Indeed, the peak at $k_z^+ = 0.02$ observed for the streamwise velocity corresponds to a wavelength $\lambda_z^+ \approx 300$. A similar shift has been noted by Tomkins & Adrian[17] in boundary layers at $Re_\tau = 426$, with the most energetic scales ranging over $200 \leq \lambda_z^+ \leq 400$ at $y^+ = 21$.

The spectra obtained from the data further from the wall, at $y^+ = 105$, or $y = 0.3\delta$ in outer units, are presented in figure 11(b), as functions of the wavenumber scaled by the half-width of the channel, $k_z h$. The velocity field is observed to be more isotropic than previously. Anisotropy however persists at low wavenumbers, since wall normal components of the velocity are less energetic than the other components for $k_z h < 7$. The spectrum is dominated by lower wavenumbers compared to the near wall spectrum. Indeed, a peak is located at $k_z h = 5.4$, corresponding to a wavelength $\lambda_z = 1.2h$, or $\lambda_z^+ \approx 420$ in wall units. This value is higher than that provided by Tomkins & Adrian from boundary layer experiments, who measured the most energetic scales around $\lambda_z \approx 0.8\delta$, at $y = 0.2\delta$,[17] with δ the boundary-layer thickness. However, the authors pointed out that the largest scales in boundary layers and in channel flows should exhibit different behaviors, since they are influenced by the geometry of the facility.

Comparison can also be made with the LES results of Bogey *et al.* for a tripped nozzle pipe flow.[29] Just downstream of the exit, the azimuthal modes of the streamwise velocity are noticed to be the most energetic at $k_\theta \delta/r_0 \approx 7$,[33] where r_0 is the pipe radius.

III.F. Wall-pressure spectra

The wall-pressure frequency spectrum $\Phi_{pp}(\omega)$, shown on figure 12, is obtained by integration of the 3-D spectrum over k_x and k_z. The axes are in logarithmic scales, and coordinates are given in wall units. The spectrum has been premultiplied by the angular frequency ω to highlight the separation between high and low frequency regions. For low frequencies, the premultiplied spectrum increases with ω, following a power law with an exponent close to 1. The spectrum reaches a peak at a non-dimensional angular frequency $\omega^+ = 0.3$, as it was observed by Hu[28] for Reynolds numbers between 360 and 1440. Then, for higher frequencies, the spectrum rapidly decreases. A slope of order ω^{-4} indicated in the figure by a blue dashed line can be noticed in a small range of frequencies $\omega^+ \approx 0.8 - 1$, which is consistent with the decay in ω^{-5} observed for Φ_{pp} in a number of boundary-layer experiments.[34] The decay becomes sharper for $\omega^+ \geq 1$, which can be attributed to the dissipative effect of the relaxation filter of the LES, whose cut-off wavenumber is $k_x \approx 2\pi/(4\Delta x)$ in the

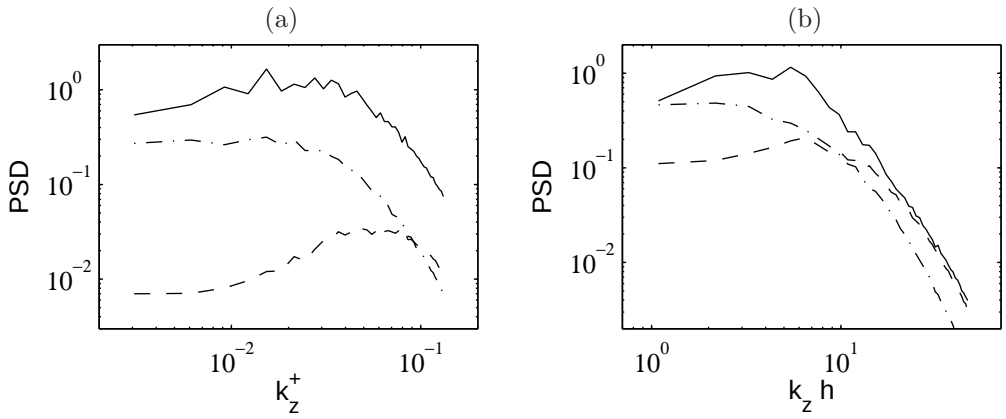

Figure 11. Power spectral density of the velocity fluctuations as functions of k_z, at (a) $y^+ = yu_f/\nu = 18$ ($y/h = 0.05$), and (b) $y^+ = 105$ ($y/h = 0.3$). ——— Φ_{uu}, – – – Φ_{vv}, – · – · Φ_{ww}.

streamwise direction. Assuming Taylor hypothesis of frozen turbulence convected at a speed roughly equal to $u_{conv} = 0.7U_c$, the non-dimensional cut-off angular frequency is equal to $\omega\nu/u_\tau^2 \approx 1.26$, which corresponds well to the frequency at which a strong decrease is observed in the figure. Finally, two peaks with narrow bandwidth appear at frequencies $\omega^+ = 0.58$ and 1.15. These peaks are related to acoustic components. Their origin will be explained with a 2-D spectrum thereafter.

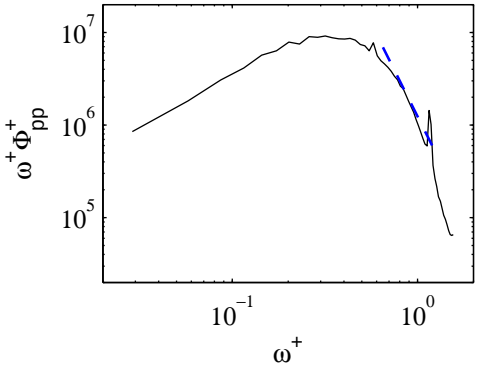

Figure 12. Power spectral density of the wall pressure fluctuations as a function of $\omega^+ = \omega\nu/u_f^2$.

A 2-D spectrum of the pressure fluctuations obtained by integration of the 3-D spectrum over k_z is presented in figure 13(a), as a function of the streamwise wavenumber k_x and angular frequency ω, scaled by the centerline velocity U_c and the channel half-width h. Similarly, integration of the 3-D spectrum over k_x provides the 2-D spectrum given in figure 13(b), as a function of the spanwise wavenumber k_z and ω. A well-known feature in wavenumber-frequency power spectra of wall-pressure fluctuations is the convective ridge, which is attributed to turbulent structures convected by the mean flow. The ridge consists of a strong peak which has been observed by early measurements such as those of Willmarth & Wooldridge,[35] and which is the basis for the construction of most wall-pressure models such as that of Corcos.[36] Since this feature arises from convective transport without any compressible effect, it has been studied in many incompressible simulations.[37–39] In figure 13(a), the convection ridge is clearly visible around wavenumbers $k_x = \omega/u_{conv}$, which are indicated by a black dashed line. The convection speed $u_{conv} = 0.7U_c$, used above for the frozen turbulence hypothesis, has been deduced from the slope of the convection ridge. It can be noted that the ridge is not visible on the $k_z - \omega$ spectrum, presented in figure 13(b). Indeed, since the flow is in the streamwise direction, no convection effect can be expected in spanwise direction. Then, the $k_z - \omega$ spectrum is symmetric with respect to $k_z = 0$.

As noted by Bull,[1] a more interesting part than the convective ridge is the low wavenumber region of the 2-D spectra, because it contributes to the structural excitation and radiated noise. The latter is generated by components contained in the supersonic region of the wavenumber-frequency spectrum, delimited by

$k_x^2 + k_z^2 \leq (\omega/c - k_x M_{conv})^2$ with $M_{conv} = u_{conv}/c$. Since the present 2-D spectra are obtained by integration over k_z or k_x, the limits of the supersonic region degenerate in $k_x = \omega/(c \pm u_{conv})$ for the $k_x - \omega$ spectrum, and in $k_z = \pm\omega/c$ for the $k_z - \omega$ spectrum. These limits, called sonic lines, are denoted by red dashed lines in figures 13(a) and (b).

The peaks found inside the supersonic region represent the footprint of the acoustic waves computed directly by the compressible LES. The two peaks previously observed on the 1-D frequency spectrum in figure 12 are found in the $k_x - \omega$ spectrum in figure 13(a) at $\omega h/U_c = 10.7$ and 21.4. A third harmonic can be noticed at $\omega h/U_c = 33$. These components do not propagate in the streamwise direction, because they are located at a streamwise wavenumber $k_x = 0$. It can be seen on the $k_z - \omega$ spectrum in figure 13(b) that two peaks are found at the same values of ω. In this case, they are located on sonic lines. The second harmonic $\omega h/U_c = 21.4$, where a peak is found on each sonic line, is especially visible. This means that these components are due to acoustic waves traveling in the spanwise direction. Apart from these spanwise modes, a greater number of peaks are found in the $k_x - \omega$ spectrum in figure 13(a), for $k_x \neq 0$ and $\omega h/U_c > 15$ in the supersonic region. For lower frequencies, the acoustic contributions do not appear, and are dominated by the convective ridge. Acoustic components are noticed at discrete values of ω and k_x or k_z, suggesting that only a limited number of acoustic modes radiate in the channel.

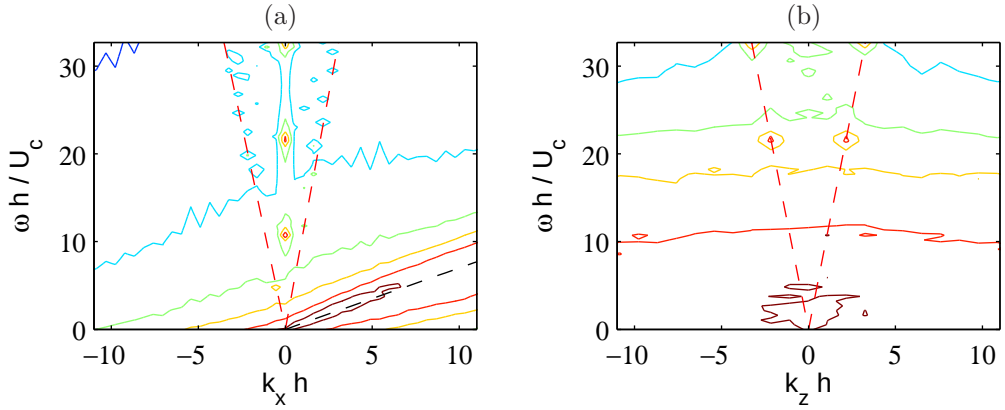

Figure 13. Power spectral density of the wall pressure fluctuations as a function of ω and (a) k_x, (b) k_z. Two consecutive isolines represent a magnitude ratio of 6.4. — — — convective wavenumber $k_x = \omega/u_{conv}$ with $u_{conv} = 0.7U_c$, — — — convected acoustic wavenumbers (a) $k_x = \omega/(u_{conv} \pm c)$, and (b)$k_z = \pm\omega/c$

IV. Conclusion

In this paper, two semi-implicit schemes of order 3, referred to as SIRK63-A and SIRK63-S, are designed for the direct noise computation of wall-bounded turbulent flows. These two schemes use the explicit scheme of Berland *et al.*[9] as explicit sub-scheme. Their respective implicit sub-schemes are unconditionally stable, and allow to perform the time integration of the flux-governing equations in the direction where the mesh is refined without decreasing the time step significantly. The damping factor and dispersion error of the SIRK63-A and SIRK63-S algorithms are inferior or similar to that of the standard Runge-Kutta scheme of order 4. These results are obtained from an acoustic test case consisting of a pulse propagating in a 2-D domain. The SIRK63-S algorithm is then used in a compressible LES of a turbulent channel flow at $Re_\tau = 360$ and $M = 0.1$. The mean and fluctuating velocity profiles are in good agreement with corresponding DNS data from the litterature. Velocity spectra are computed from the LES data, at two different distances to the wall. It reveals that the spanwise arrangement of the turbulent structures is slightly larger in this channel flow case compared to the results observed in turbulent boundary layers.[17] Wall pressure fluctuations are also considered in the present study. In particular, the wavenumber-frequency spectrum exhibits the classical convective ridge, and some acoustic components are found in the low-wavenumber region. This point illustrates the ability of the compressible LES to compute directly the noise generated by a turbulent wall-bounded flow.

Appendix : six-stage fourth-order semi-implicit Runge-Kutta schemes

In this appendix, the coefficients of the implicit part of the semi-implicit algorithms are listed in table 3 for the SIRK63-S scheme, and in table 4 for the SIRK63-A scheme. The coefficients of their explicit part are also given in table 5. They are equal to the coefficients of the scheme RK46-Ber of Berland *et al.*[9]

Table 3. Coefficients of the implicit part of the SIRK63-S scheme.

	0.41					
	-0.050847598260407	0.41				
	-0.732843054288974	0.488808741097800	0.41			
$a_{ij}^{[I]}$	0.518289378427379	-1.277080692402156	0.558980743308365	0.41		
	-0.802531364350514	0.646260865229491	0.497772202911395	-0.379275265944952	0.41	
	-0.518537243124588	0.051438098423723	0.611601988166285	0.227118479918187	0.120091948181429	0.41
$b_i^{[I]}$	0.971001746640224	-1.272664996516041	1.282112737365169	-1.209258255434315	0.958808767944964	0.27

Table 4. Coefficients of the implicit part of the SIRK63-A scheme.

	0					
	-0.212081394856242	0.245				
	-0.506934417330455	0.511286140669274	0.245			
$a_{ij}^{[I]}$	-3.2	3.622080130757558	-0.200168425700507	0.245		
	0.273655978647576	-0.810460387252415	1.516528920894552	-0.642694098243515	0.245	
	0.272572117804249	0.001343810878341	-0.020976057113187	-0.117426001935445	0.466739114149427	0.245
$b_i^{[I]}$	0.971001746640224	-1.272664996516041	1.282112737365169	-1.209258255434315	0.958808767944964	0.27

Table 5. Coefficients of the RK46-Ber scheme of Berland *et al.*,[9] corresponding to the explicit part of the SIRK63-S and SIRK63-A schemes.

	0					
	0.032918605145602	0				
	-0.573905274855897	0.823256998199009	0			
$a_{ij}^{[E]}$	-0.114172035573537	0.199552791728150	0.381530948900243	0		
	-0.293732375804120	0.443156103274586	0.232514473389434	0.200092213184021	0	
	1.973193167196099	-2.632303480923729	2.113827764673696	-2.326045509877871	1.718581042714500	0
$b_i^{[E]}$	0.971001746640224	-1.272664996516041	1.282112737365169	-1.209258255434315	0.958808767944964	0.27

Acknowledgments

The first author is grateful to the Direction Générale de l'Armement (DGA) and the Centre National de la Recherche Scientifique (CNRS) for financial support. This work was granted access to the HPC resources of the Institut du Développement et des Ressources en Informatique Scientifique (IDRIS) under the allocation 2011-020204 made by GENCI (Grand Equipement National de Calcul Intensif). The authors would like to thank Olivier Marsden for his help on the parallelization of the code with the OpenMP library.

References

[1]Bull, M.K., "Wall-pressure fluctuations beneath turbulent boundary layers: some reflections on forty years of research," *Journal of Sound and Vibration* Vol. 190, No. 3, 1996, pp. 299-315

[2]Tam, C.K.W. and Webb, J.C., "Dispersion-relation-preserving finite difference schemes for computational acoustics," *J. Comput. Phys.*, Vol. 107, No. 2, 1993, pp. 262-281.

[3]Lele, S.K., "Compact finite difference schemes with spectral-like resolution," *J. Comput. Phys.*, Vol. 103, No. 1, 1992, pp. 16-42.

[4]Bogey, C. and Bailly, C., "A family of low dispersive and low dissipative explicit schemes for flow and noise computations," *J. Comput. Phys.*, Vol. 194, No. 1, 2004, pp. 194-214.

[5]Runge, C., "Über die numerische Auflösung von Differentialgleichungen", *Mathematische Annalen*, Vol. 46, 1895, pp. 167-178.

[6]Bashforth, F. and Adams, J.C., "An attempt to test the theories of capillary action by comparing the theoretical and measured forms of drops of fluid, with an explanation of the method of integration employed in constructing the tables which give the teoretical forms of such drops," *Cambridge University Press*, 1883

[7]Hu, F.Q., Hussaini, M.Y. and Manthey, J.L., "Low-dissipation and low-dispersion Runge-Kutta schemes for computational acoustics," *J. Comput. Phys.* Vol. 124, 1996, pp. 177-191.

[8]Stanescu, D., "2N-Storage Low Dissipation and Dispersion Runge-Kutta Schemes for Computational Acoustics," *J. Comput. Phys.* Vol. 143, 1998, pp. 674-681.

[9]Berland, J., Bogey, C. and Bailly, C., "Low-dissipation and low-dispersion 4th-order Runge-Kutta algorithm," *Comp. & Fluids*, Vol. 35, 2006, pp. 1459-1463.

[10]Wu, X. and Moin, P., "Direct numerical simulation of turbulence in a nominally zero-pressure-gradient flat-plate boundary layer," *J. Fluid Mech.*, Vol. 630, 2009, pp. 5-41.

[11]Simens, M.P., Jiménez, J., Hoyas, S. and Mizuno, M., "A high-resolution code for turbulent boundary layers," *J. Comput. Phys.* Vol. 228, 2009, pp. 4218-4231.

[12]Asher, U.M., Ruuth, S.J. and Spiteri, R.J., "Implicit-explicit Runge-Kutta methods for time-dependent partial differential equations," *Appl. Numer. Math.* Vol. 25, 1997, pp. 151-167.

[13]Calvo, M.P., de Frutos, J. and Novo, J., "Linearly implicit Runge-Kutta methods for advection-reaction-diffusion equations," *Appl. Numer. Math.* Vol. 37, 2001, pp. 535-549.

[14]Zhong, X., "Additive semi-implicit Runge-Kutta methods for computing high-speed nonequilibrium reactive flows," *J. Comput. Phys.* Vol. 128, No. 1, 1996, pp. 19-31.

[15]Kennedy, C.A. and Carpenter, M.H., "Additive Runge-Kutta schemes for convection-diffusion-reaction equations," *Appl. Num. Math.* Vol. 44, 2003, pp. 139-181.

[16]Suh, J., Frankel, S.H., Mongeau, L. and Plesniak, M.W., "Compressible large eddy simulations of wall-bounded turbulent flows using a semi-implicit numerical scheme for low Mach number aeroacoustics," *J. Comput. Phys.* Vol. 215, No. 2, 2006, pp. 526-551.

[17]Tomkins, C.D. and Adrian, R.J., "Energetic spanwise modes in the logarithmic layer of a turbulent boundary layer," *J. Fluid Mech.*, Vol. 545, 2005, pp. 141-162

[18]Jiménez, J., Hoyas, S., Simens, M. and Mizuno, M., "Turbulent boundary layers and channels at moderate Reynolds numbers," *J. Fluid Mech.* Vol. 657, 2010, pp. 335-360

[19]Curle, N., "The influence of solid boundaries upon aerodynamic sound," *Proc. R. Soc. Lond., A*, Vol. 231, 1955, pp. 505-514.

[20]Powell, A., "Aerodynamic noise and the plane boundary," *J. Acoust. Soc. Am.*, Vol. 32, No. 8, 1960, pp. 982-990.

[21]Ffowcs Williams, J.E. and Hawkings, D.L., "Sound generation by turbulence and surfaces in arbitrary motion," *Phil. Trans. R. Soc. Lond., A*, Vol. 264, 1969, pp. 321-342.

[22]Hu, Z.H., Morfey C.L. and Sandham, N.D., "Sound radiation in turbulent channel flows," *J. Fluid Mech.*, Vol. 475, 2003, pp. 269-302.

[23]Hu, Z.H., Morfey C.L. and Sandham, N.D., "Sound radiation from a turbulent boundary layer," *Phys. Fluids*, Vol. 18, No. 9, 2006, 098101.

[24]Gloerfelt, X., "The link between wall pressure spectra and radiated sound from turbulent boundary layers," *16th AIAA/CEAS AeroAcoustics Conference* 7-9 June 2010, Stockholm, Sweeden.

[25]Alexander, R., "Diagonally implicit Runge-Kutta methods for stiff O.D.E.s" *SIAM J. Numer. Anal.*, Vol. 14, No. 6 1977, pp. 1006-1021.

[26]J. Kim, J., Moin, P. and Moser, R., "Turbulence statistics in fully developed channel flow at low Reynolds number," *J. Fluid Mech.*, Vol. 177, 1987, pp. 133-166.

[27]Schlatter, P. and Orlu, R., "Assessment of direct numerical simulation data of turbulent boundary layers," *J. Fluid Mech.*, Vol. 659, 2010, pp. 116-126.

[28]Hu, Z.H., Morfey C.L. and Sandham, N.D., "Wall pressure and shear stress spectra from direct simulations of channel flow," *AIAA J.* Vol. 44, No. 7, 2006, pp. 1541-1549.

[29]Bogey, C., Marsden, O., and Bailly, C., "Large-Eddy Simulation of the flow and acoustic fields of a Reynolds number 10^5 subsonic jet with tripped exit boundary layers," *Phys. Fluids*, Vol. 23, No. 3, 2011, 035104.

[30]Bogey, C. and Bailly, C., "Large Eddy Simulations of transitional round jets: influence of the Reynolds number on flow development and energy dissipation," *Phys. Fluids*, Vol. 18, No. 6, 2006, 065101.

[31]Moser, R.D., Kim, J. and Mansour, N., "Direct numerical simulation of turbulent channel flow up to $Re_\tau = 590$," *Phys. Fluids*, Vol. 11, No. 4, 1999, pp. 943-945.

[32]Kline, S.J., Reynolds, W.C., Schraub, F.A. and Runstadler, P.W., "The structure of turbulent boundary layers," *J. Fluid Mech.* Vol. 30, 1967, pp. 741-773.

[33]Bogey, C., Marsden, O. and Bailly, C., "On the spectra of nozzle-exit velocity disturbances in initially nominally turbulent, transitional jets," *Phys. Fluids* Vol. 23, No. 9, 2011, 091702.

[34]Goody, M.C. and Simpson R.L., "Surface pressure fluctuations beneath two- and three-dimensional turbulent boundary layers," *AIAA Journal* Vol. 38, No. 10, 2000, pp. 1822-1831.

[35]Willmarth, W.W. and Wooldridge, C.E., "Measurements of the fluctuating pressure at the wall beneath a thick turbulent boundary layer," *J. Fluid Mech.* Vol. 14, 1962, pp. 187-210.

[36]Corcos, G.M., "Resolution of pressure in turbulence," *J. Acoust. Soc. Am.* Vol. 35, 1963, pp. 192-199.

[37]Hu, Z.H., Morfey C.L. and Sandham, N.D., "Aeroacoustics of wall-bounded turbulent flows," *AIAA Journal* Vol. 40, No. 3, 2002, pp. 465-473.

[38]Choi, H. and Moin, P., "On the space-time characteristics of wall-pressure fluctuations," *Phys. Fluids A* Vol. 2, No. 8, 1990, pp. 1450-1460.

[39]Viazzo, S., Dejoan, A. and Schiestel, R., "Spectral features of the wall-pressure fluctuations in turbulent wall flows with and without perturbations using LES," Int. J. Heat and Fluid Flow Vol 22, 2001, pp. 39-52.